

FENNECS: a novel particle-in-cell code for simulating the formation of magnetized non-neutral plasmas trapped by electrodes of complex geometries

G. Le Bars^{a,*}, S. Guinchard^a, J. Loizu^a, J.-Ph. Hogge^a, S. Alberti^a, F. Romano^a,
J. Genoud^a, A. Cerfon^b

^a *Ecole Polytechnique Fédérale de Lausanne (EPFL), Swiss Plasma Center (SPC), CH-1015
Lausanne, Switzerland*

^b *Courant Institute of Mathematical Sciences, New York University, New York, NY 10012 USA*

Abstract

This paper presents the new 2D electrostatic particle-in-cell code FENNECS developed to study the formation of magnetized non-neutral plasmas in geometries with azimuthal symmetry. This code has been developed in the domain of gyrotron electron gun design, but solves general equations and can be applied in other domains of plasma physics. FENNECS is capable of simulating electron-neutral collisions using a Monte Carlo approach and considers both elastic and inelastic (ionization) processes. It is also capable of solving the Poisson equation on domains with arbitrary geometries with either Dirichlet or natural boundary conditions. The Poisson solver is based on a meshless Finite Element Method, called web-splines, based on b-splines of any order, and used for the first time in the domain of plasma physics. In addition, the effect of fast ions colliding with the electrodes and causing ion induced electron emission at the electrode surfaces has been implemented in the code. In this paper, the governing equations solved by FENNECS and the numerical methods used to solve them are presented. A number of verification cases are then reported. Finally, the parallelization scheme used in FENNECS and its parallel scalability are presented.

Keywords: particle-in-cell; finite element methods; web-splines; Monte Carlo; non-neutral plasma; gyrotron

*Corresponding author.
E-mail address: guillaume.lebars@epfl.ch

PROGRAM SUMMARY

Program Title: FENNECS

CPC Library link to program files: (to be added by Technical Editor)

Developer's repository link: <https://c4science.ch/source/fennecs/>

Code Ocean capsule: (to be added by Technical Editor)

Licensing provisions(please choose one): MIT

Programming language: Fortran 90 and C

Nature of problem:

Self-consistent formation and evolution of magnetized electrostatic non-neutral plasmas confined in geometries with azimuthal symmetry and arbitrary radial and axial profile for the enclosing electrodes. The clouds can be formed by a volumetric source or a by ionization of a residual neutral gas present in the vacuum vessel. In addition, the effect of ion induced electron emission due to fast ions colliding with the enclosing electrodes are considered.

Solution method:

The code uses a particle-in-cell approach with a Monte Carlo algorithm to simulate the electron neutral collisions and the ion induced electron emission due to fast ions colliding with the electrodes of the geometry. The magnetic field is imposed externally and the electrostatic potential is solved using a novel web-spline method based on b-splines of any order. The particle are advanced in space and time using the Boris algorithm.

Additional comments including restrictions and unusual features:

The code is parallelized with shared and distributed memory using respectively OpenMP and MPI libraries.

1. Introduction

The understanding of the dynamics of non-neutral plasmas is relevant to many fields in physics and engineering, from extremely cold and low density plasmas in elementary particle physics [1], to high-energy and high density plasmas in particle accelerators [2] or microwave sources [3]. These plasmas possess interesting stability properties that allow them to be stored for long periods of time ranging from hours to days [4] and allow the accumulation of antimatter charged particles. They play a central role in the study of antimatter (for example the effect of gravity on anti-Hydrogen [5, 6]), or in the accumulation and storage of positrons necessary to study electron-positron plasmas [7]. In the domain of microwave sources, non-neutral plasmas can be used to generate or amplify RF waves [3], but they can also form in the microwave device at undesired places, hindering the normal operation of the source. For example in some high power gyrotrons used to heat

the electrons of magnetically confined fusion plasmas, electron clouds can form in the electron gun region of the device, preventing their nominal operation [8, 9]. These clouds are formed due to the presence of potential wells generated by the combination of externally applied electric and magnetic fields and are similar in nature to the ones characterizing Penning traps [1, 9, 10]. Due to their high kinetic energy, the trapped electrons can ionize the residual neutral gas present in the gun and lead to high density clouds that can cause damaging currents between the accelerating electrodes of the gun and can lead to arcing events. To understand the conditions of formation of these clouds and their evolution, a particle-in-cell code called FENNECS (Finite Element Non-Neutral Electron Cloud Simulator) has been developed and is the subject of this publication.

Current codes considering neutral and non-neutral plasma discharges are either proprietary (LSP [11], MAGIC [12]), or are limited to simple electrode geometries (NINJA [13]) due to the method used to solve Poisson equation. In the domain of gyrotrons, electron gun simulations are carried out with codes capable of simulating the complex geometry of the gun. However, the most common codes such as EGUN [14], ESRAY [15], DAPHNE [16] or ARIADNE++ [17] do not consider electron neutral collisions and assume a beam-optics framework, which considers the long time scale evolution and neglects the fast electrostatic modes that can arise in high density electron clouds. Another candidate, the WARP [18–20] code, is both capable of simulating electron neutral collisions and the complex electrodes geometries used in gyrotron electron guns. However, due to the finite difference method on staggered grids used to solve Poisson’s equation, simulations of complex geometries require potentially costly grid refinements.

The 2D electrostatic axisymmetric particle-in-cell code FENNECS presented in this paper considers a novel Finite Element Method (FEM) that allows the exact definition of electrodes geometry and somewhat decouples the grid definition and the geometry of interest when solving for the electrostatic potential. This method has been successfully used in several domains of physics, for example to solve elastic deformation problems [21], electromagnetic wave propagation in wave-guides [22], or the stationary Stokes problem [23], and is used for the first time in plasma physics, to the best of the authors knowledge [24, 25]. The code is also capable of simulating electron neutral collisions, considering elastic and inelastic (ionization) collisions, and resolves the fast time-scale plasma waves and electron cyclotron motion. This is of great importance for simulating high-density trapped electron clouds for which the Brillouin ratio, defined as $f_b = 2\omega_{pe}^2/\Omega_{ce}^2$ is close to one. Here, $\omega_{pe}^2 = e^2 n_e / \epsilon_0 m_e$ is the electron plasma frequency squared

and $\Omega_{ce} = eB/m_e$ the electron cyclotron frequency. e and m_e are, respectively, the electron charge and mass, n_e is the electron density, B is the magnetic field amplitude, and ϵ_0 is the vacuum permittivity. The magnetic fields generated by the electron clouds are neglected in front of the important externally applied magnetic field since the strong externally applied magnetic field dominates the dynamics. This code has already been successfully used to study the self-consistent formation of trapped electron clouds in gyrotron electron guns and to derive scaling laws for the electron cloud density and resulting current as a function of external parameters [9]. In the same context, FENNECS was successfully validated against experimental measurements [26]. The code is currently used to study gyrotron electron guns. However, the authors believe that the governing equations are sufficiently general that it could be used in the domain of Penning traps [1], or be easily adapted to study cathodic arcs [27]. In addition, the code and its dependencies are open-source, which facilitates its modification, enables further improvements, and simplifies the beginning of new collaborations.

The goal of the present paper is to present the FENNECS code and capabilities, as well as the numerical methods used. After the introduction, Sec.2 describes the physical model implemented in FENNECS. In Sec.3, the numerical methods used to simulate different physical phenomena are described, and special care is taken to describe the novel FEM solver based on weighted extend b-splines (web-splines). The Monte Carlo methods used to simulate electron-neutral collisions and ion induced electron emission on the electrode surfaces are also described. In Sec.4, a set of verification test cases confirming the correct implementation of the governing equations is also presented. The parallelization schemes are described and the scalability of the code using domain decomposition is presented in Sec.5. Finally, a summary of the paper and its conclusions follow.

2. Physical model

2.1. Governing equations

FENNECS is an axisymmetric 2D3V electrostatic particle-in-cell code that solves the Boltzmann-Poisson system for an electron distribution function $f(\vec{r}, \vec{v}, t)$ and the electrostatic potential $\phi(\vec{r}, t)$ with the addition of electron-neutral collision operators. The neutral gas is considered as a cold background gas of uniform density n_n . Only one neutral gas species is considered, and it is assumed that n_n does not change in time. In the current model, only elastic and single ionization collisions are considered with their respective collision cross-sections σ_{ela} and σ_{io} . This choice is supported by the fact that, due to the large radial electric field

in gyrotron electron guns, the newly formed ions are lost on time-scale $\tau_{ion,loss}$ much smaller than the second ionization collision time scale. Similarly, due to the large electron kinetic energies (more than several hundred eV), the collision time-scales for excitation of the neutral gas are at least one order of magnitude larger than both the elastic and single ionization time-scales and are therefore neglected [9, 28]. In elastic and ionization collisions, we assume anisotropic scattering cross-sections using a screened-Coulomb scattering cross-section [29]. For an ionization event, the remaining kinetic energy after collision (initial kinetic energy minus the ionization energy) is split between the freed and the incoming electron using a double differential cross-section $\frac{\partial^2 \sigma_{io,sec}}{\partial \Omega \partial E_p}$ for the energy of the secondary electron, and a second double differential cross-section $\frac{\partial^2 \sigma_{io,sca}}{\partial \Omega \partial E_p}$ for the energy of the scattered electron. These cross-sections depend on the solid scattering angle Ω and the incoming electron energy E_p [30]. The two double differential cross-sections are defined such that, in ionization events, the total energy is conserved $E_p = E_{io} + E_{sca} + E_{sec}$. Here, E_{io} is the first ionization energy of the neutral gas, E_{sca} is the energy of the scattered electron and E_{sec} is the energy of the secondary electron.

The magnetic field \vec{B}_0^{ext} is imposed externally, and the magnetic field generated by the electron cloud is neglected. Perfectly absorbing boundary conditions for the particles are used at the electrodes, thereby representing a loss term L_{wall} . In addition, a volumetric seed source S_{seed} can be imposed, and electron emission due to ions impacting the electrode surfaces can be simulated, introducing a surface source S_{IEEE} . In this case, the Boltzmann equation becomes

$$\begin{aligned}
& \left[\frac{\partial}{\partial t} + \vec{v} \cdot \frac{\partial}{\partial \vec{r}} - \frac{e}{m_e} \left(\vec{E} + \vec{v} \times \vec{B}_0^{\text{ext}}(\vec{r}) \right) \cdot \frac{\partial}{\partial \vec{v}} \right] f(\vec{r}, \vec{v}, t) = \\
& + n_n |\vec{v}| \int \frac{d\sigma_{\text{ela}}(|\vec{v}|)}{d\Omega} [f(\vec{r}, \vec{v}'(\Omega), t) - f(\vec{r}, \vec{v}, t)] d\Omega \\
& + \frac{n_n |\vec{v}|}{E} \left(\int_{E+E_{io}}^{2E+E_{io}} \int E_p \frac{\partial^2 \sigma_{io,sec}}{\partial \Omega \partial E_p} f(\vec{r}, \vec{v}'(\Omega), t) d\Omega dE_p \right. \\
& + \left. \int_{2E+E_{io}}^{\infty} \int E_p \frac{\partial^2 \sigma_{io,sca}}{\partial \Omega \partial E_p} f(\vec{r}, \vec{v}'(\Omega), t) d\Omega dE_p \right) \\
& - n_n |\vec{v}| \sigma_{io}(|\vec{v}|) f(\vec{r}, \vec{v}, t) \\
& + S_{seed} + S_{IEEE} - L_{wall}.
\end{aligned} \tag{1}$$

Here, Ω is the solid scattering angle; \vec{v}' is the electron velocity that is scattered by a solid angle Ω to \vec{v} [31]; $E = m_e |\vec{v}|^2 / 2$ is the electron energy at velocity \vec{v} . On the

right hand side, the first term accounts for the scattering by elastic collisions [31], the second term describes the emission of secondary electrons by ionization, the third term accounts for the scattering of incoming electrons during an ionization collision and the fourth term describes the electrons removed from the distribution by ionization [32]. The electric potential ϕ is solved self-consistently using Poisson's equation

$$\nabla^2 \phi(\vec{r}, t) = -\frac{\rho}{\epsilon_0} = \frac{e}{\epsilon_0} \int f(\vec{r}, \vec{v}, t) d^3\vec{v} \quad (2)$$

and considering the boundary conditions imposed by the electrodes. At the electrodes, in addition to fixed potentials imposed by ideal power supplies, the resistive and capacitive effects of a non-ideal power-supply can be simulated (see section 3.5).

2.2. Normalizations

To improve the numerical precision of the code, all the physical quantities are normalized by physical constants relevant to the problem. To this end, four reference quantities are used: B_0 , an input parameter usually set to the maximum amplitude of the magnetic field in the simulation domain; c , the speed of light in vacuum; e , the electron charge; and m_e , the electron mass. The time is normalized by the inverse of the cyclotron frequency $t_N = 1/\Omega_{ce} = m_e/eB_0$, velocities are normalized to $v_N = c$, lengths are normalized to $r_N = v_N/t_N$, the magnetic field is given in units of $B_N = B_0$, and the electric potential and fields are respectively normalized by $\phi_N = B_N v_N r_N$ and $E_N = v_N B_N$.

2.3. Geometries of interest

As FENNECS is a 2D axisymmetric code, it is capable of simulating geometries with an azimuthal symmetry. Namely, in cylindrical coordinates (r, θ, z) all fields can depend on r and z but not on θ . For gyrotron electron guns, the typical geometry of interest, as represented in Figure 1, is composed of a coaxial cathode and an outer cylindrical anode described by an arbitrary radial profile $r(z)$. However, the code is more flexible in the definition of the electrodes and multiple concentric electrode rings can be defined. Similarly, regions where only the outer electrode is present are also possible. This is important to simulate all types of gyrotron electron guns, but can also be useful to study non-neutral plasmas in other physical settings. In addition independent potentials can be applied to each simulated electrodes. Furthermore, the particles are subjected to an axisymmetric

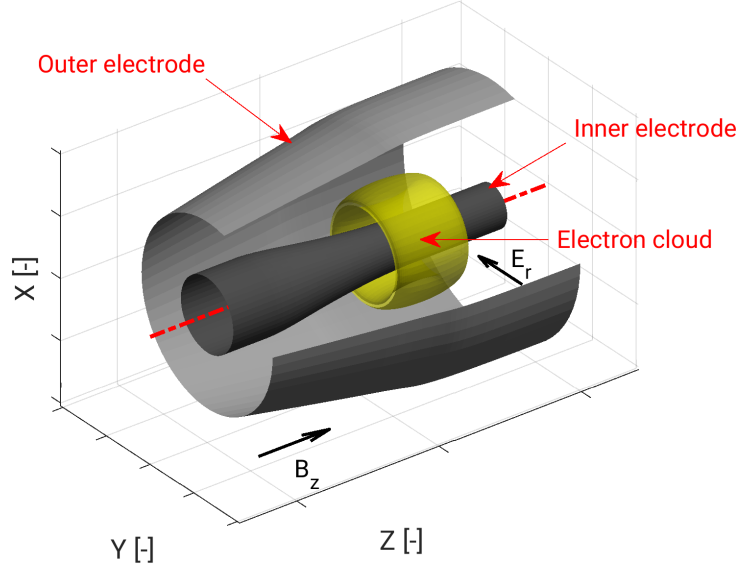


Figure 1: Typical geometry of interest used in FENNECS. The yellow ring represents an example of an electron plasma cloud. The gray/black parts are the electrodes on which a fixed potential can be applied. The red dotted-dashed line highlights the axis of symmetry.

external magnetic field with both radial and axial components. In the configurations typical of gyrotron guns, the electron clouds usually have an annular shape (see Figure 1) confined axially by magnetic mirrors, due to the electrons large perpendicular velocity, or by electrostatic potential wells imposed externally [9, 10]. However, cylindrical clouds can also be simulated.

2.4. Time scale separation

Typical electron clouds trapped in gyrotron electron guns are subject to physical phenomena happening on various time-scales. These can span up to ten orders of magnitude, between the fast electron cyclotron motion at Ω_{ce} , and the slow ionization collision frequency f_{i0} and effective elastic collision frequency for momentum exchange f_d , as illustrated in Figure 2. This large time scale separation prevents the complete simulation of all the time-scales due to the numerical cost of the task. However, as $f_{i0} = n_n < \sigma_{i0} v >$ and $f_d = n_n < \sigma_{ela} v >$ are linearly proportional to n_n , the collision time-scales can be shortened by considering, in the simulations, an increased neutral gas pressure $n_{n,simu} = \alpha n_{n,phys}$ compared to the physical pressure of interest [9, 26]. This factor $\alpha > 1$ must be selected such that a sufficient time-scale separation is kept between the slow and fast time-scales,

namely such that $f_{io}, f_d \ll f_{||}$. Here, $f_{||} \approx v_{||}/L$ is the electron bounce frequency in the trap of length L along the magnetic field lines, and $v_{||}$ is the electron velocity parallel to the magnetic field line. The simulation characteristic times of particle losses can then be rescaled to the physical time-scales using the same parameter α .

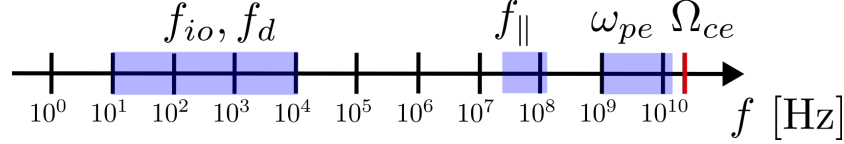


Figure 2: Relevant time scales for electron clouds of interest simulated by FENNECS. f_{io} and f_d are the ionization collision frequency and the effective elastic collision frequency for momentum exchange; $f_{||} \approx v_{||}/L$ is the electron bounce frequency in the trap of length L along the magnetic field lines; ω_{pe} is the electron plasma frequency; Ω_{ce} is the electron cyclotron frequency. The blue shaded area indicates the range of possible time scales for $n_e \approx 10^{14} \rightarrow 10^{17} \text{m}^{-3}$ and $n_n \approx 10^{13} \rightarrow 10^{17} \text{m}^{-3}$. The red line give Ω_{ce} for $B = 0.3 \text{ T}$.

3. Numerical methods

To solve the Boltzmann equation (1) and the Poisson equation (2), the particle-in-cell method is employed. The distribution function f is sampled using a finite number of macro particles i at position \vec{r}_i with velocity \vec{v}_i and each representing N_i electrons such that

$$f(\vec{r}, \vec{v}, t) = \sum_i N_i \delta(\vec{r} - \vec{r}_i) \delta(\vec{v} - \vec{v}_i). \quad (3)$$

Here $\delta(\vec{x})$ is the Dirac delta function.

3.1. Particle trajectory: Boris algorithm

To advance in time the macro-particle positions and velocities, according to the left hand side of Boltzmann equation (1), the Boris algorithm is used [33]. This method was selected for its simplicity and reliability, and for its capability of integrating both classical and relativistic trajectories with very little change in the code. This allows the user of FENNECS to select at run-time if the classical or relativistic Newton's equation is solved during the simulations, by means of an input flag.

3.2. Magnetic field

The magnetic field is imposed externally assuming azimuthal symmetry. It is also assumed that the external magnetic field amplitude is large enough so that the contribution from the electron cloud current can be neglected. It can be defined either using an analytical magnetic field vector potential that, e.g., approximates a magnetic mirror close to the magnetic axis, as described in Sec.4.2, or it can be calculated on a grid using standard Biot-Savart solvers and be used as an input for the simulations. The magnetic field is then interpolated using third order b-splines to the FEM solver grid points. Finally, at the particle position, the magnetic field is computed using linear interpolation from the FEM grid points values to reduce the computational cost of the evaluation. The need for b-spline interpolation comes from the fact that the Biot-Savart solver is currently run using an external code and do not necessarily guarantee that the grid points of this solver correspond to the grid-points of the FEM solver, especially when the FEM grid needs to be adapted, or the simulation domain needs to be changed. This induces some imprecision on the value of the magnetic field that remains acceptable if the Biot-Savart solver grid is sufficiently fine. However, there are plans to include the magnetic field solver directly in FENNECS to avoid the b-spline interpolation step.

3.3. Poisson: Web-spline method

The Poisson equation, for a scalar field ϕ and a source term Q , is solved on the domain D , closed by boundaries ∂D , using a Finite Element Method (FEM) based on bivariate b-splines of any order [25, 34, 35]. Dirichlet boundary conditions are imposed on boundaries ∂D_i and Neumann boundary conditions are imposed on boundaries ∂D_k such that:

$$-\nabla^2 \phi = Q \text{ in } D, \phi = g_i \text{ on } \partial D_i, \nabla_{\perp k} \phi = 0 \text{ on } \partial D_k, \quad (4)$$

where $\nabla_{\perp k}$ denotes the normal derivative perpendicular to ∂D_k . To define these boundary conditions on curved surfaces, the web-spline method is used for the first time in plasma physics, to the authors knowledge [24, 25]. This paper will be limited to the description of the method and of the points necessary for the implementation. Details regarding the numerical stability and accuracy of the method can be found in references [24, 25].

To derive a variational formulation, the electric potential ϕ is first rewritten to eliminate the inhomogeneous boundary conditions by setting

$$\phi = u + \tilde{g}, \quad (5)$$

with u a function that vanishes on ∂D_i and \tilde{g} an extension of the Dirichlet boundary conditions g to all D . \tilde{g} can be set to any smooth function such that $\tilde{g}(\vec{x}) = g_i(\vec{x}) \forall \vec{x} \in \partial D_i$. The Poisson equation is then multiplied by a test function ψ and integrated over D leading to the weak formulation:

$$\int_D \nabla u \nabla \psi = \int_D (Q\psi - \nabla \tilde{g} \nabla \psi). \quad (6)$$

To construct the Ritz-Galerkin approximation of the solution, the function ψ is taken to be a set of n_b basis polynomials Ψ_l^m of degree m with compact support on mesh cells of D , and the solution is approximated by a function ϕ_h such that

$$u_h = \sum_{l=1}^{n_b} u_l \Psi_l^m. \quad (7)$$

To ensure by construction that the Dirichlet boundary conditions are respected, the basis functions Ψ_l^m are defined such that they are 0 on ∂D_i . Solving the Ritz-Galerkin approximation of the solution then reduces to solving a system of linear equations for the coefficients u_l :

$$\overleftrightarrow{A} \cdot \vec{u} = \vec{\lambda}, \quad (8)$$

with \overleftrightarrow{A} a matrix with coefficients

$$A_{lk} = \int_D \nabla \Psi_l^m \nabla \Psi_k^m, \quad (9)$$

and $\vec{\lambda}$ a vector with coefficients

$$\lambda_l = \int_D Q \Psi_l^m - \nabla \tilde{g} \nabla \Psi_l^m. \quad (10)$$

One can define a set of basis functions Ψ_l^m using weighted b-splines by defining a smooth geometric weight function w such that $w(x) = 0 \forall x \in \partial D_i$, and w is positive inside the domain $D/\partial D_i$ and negative outside of D . In this case: $\Psi_l^m \equiv w b_{l,h}^m$, with $b_{l,h}^m$ the n-variate tensor product of b-spline of degree m , with grid width h , and support $(l_1, \dots, l_n)h + [0, m+1]^n h$. Since the grid is regular (h is the same for all b-splines of the basis), the index h will be neglected for the rest of the paper. The weighted b-spline method is known to show bad numerical convergence as the grid width is reduced due to a strong increase of the condition

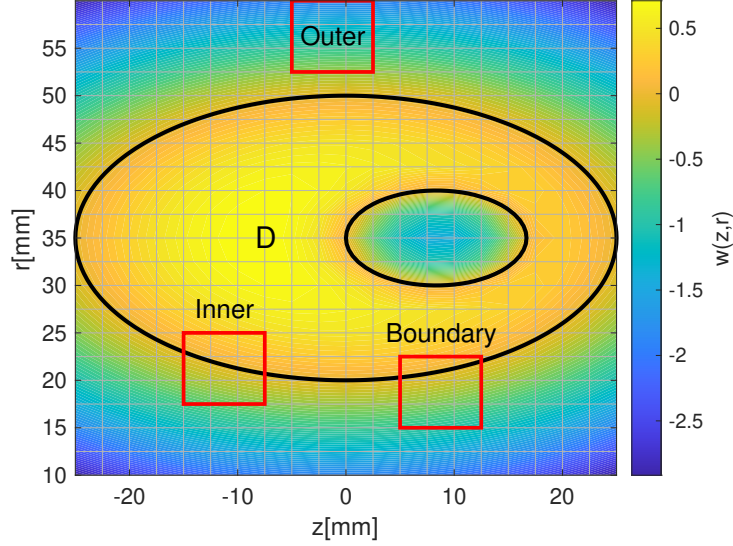


Figure 3: Geometric weight w and domain boundary for the test case presented in section 4.1 (black). The gray lines show the FEM grid, and the red squares show the boundary of the support of 3 types of quadratic b-splines.

number of the Ritz-Galerkin matrix [24]. This problem comes from the effect of boundary b-splines whose intersection between their support and the simulation domain becomes small. To alleviate this problem, Höllig and co-authors [24] combined boundary and inner b-splines to form a new basis called the web-spline basis.

To understand the web-spline basis, it is necessary to define inner, outer, and boundary b-splines, depending on the intersection between the support of the b-spline and the domain D . Inner b-splines need to have at least one grid-cell in their support that is fully inside D ; for outer b-splines, the intersection between their support and D is \emptyset ; and boundary b-splines are all the other b-splines. An example of this classification is represented in Figure 3, using the geometry defined in subsection 4.1 and quadratic b-splines. For the rest of this section, the ensemble L of inner b-splines are identified as b_l^m using the subscript l and the ensemble K of boundary b-splines are identified as b_k^m using the subscript k .

A web-spline basis $\Psi_{l,web}^m$ is defined by combining boundary and inner b-splines while keeping the correct approximation order of the initial b-spline space. To this end, the approximated solution u_h is separated between the contribution of

internal and boundary b-splines

$$u_h = \sum_{l \in L} u_l b_l^m + \sum_{k \in K} u_k b_k^m. \quad (11)$$

According to Marsden's identity [36], if u_h is a polynomial of degree $\leq m$ the coefficients u_l and u_k can be calculated by a polynomial $\tilde{u}(i) = u_i$ of degree $\leq m$ dependent on the spline index i . In this case, the outer coefficients u_k can be interpolated, for the n -variate b-splines in a space of dimension n , from any $(m+1)^n$ inner indices without affecting the approximation power of the spline space. In practice, the interpolant indices are taken as the closest $(m+1)^n$ inner indices l , and the coefficients u_k are interpolated using Lagrange polynomials such that

$$u_k = \sum_{l \in L} u_l e_{lk}. \quad (12)$$

This assumes that the grid width h is sufficiently small for this list to exist. The coefficients e_{lk} are defined as

$$e_{lk} = \prod_{v=1}^n \prod_{\mu=0}^m \frac{k_v - p_v - \mu}{l_v - p_v - \mu}, \quad (13)$$

with n the dimension of the b-spline space and p_v the lower index in each dimension of the inner interpolating splines. In addition to the interpolation of the external coefficients u_k , the web-spline basis is also rescaled by the weight evaluated at x_l , the center of a grid cell belonging to the support of b_l^m and fully inside D . The final web-spline basis is finally defined as

$$\Psi_{l,web}^m = \frac{w}{w(x_l)} \left[b_l^m + \sum_{k \in K(l)} e_{lk} b_k^m \right], \quad (14)$$

with $K(l)$ the ensemble of boundary b-splines for which the inner b-spline l is used to interpolate u_k . The Ritz-Galerkin matrix obtained using this new web-spline basis has a condition number which is reduced and remains stable as the grid width is reduced. This greatly improves the numerical stability of the finite element method and allows for arbitrary small grid width. In addition, this method allows to keep a regular grid and thus greatly simplifies the localization of the particles in the grid and facilitates the code parallelization with domain decomposition.

In FENNECS, since the distribution function is sampled with point-like macro particles defined with δ functions, the evaluation of the first term of λ_l is straightforward. This term becomes, for an electron distribution function,

$$\begin{aligned}\int_D Q\Psi_l^m &= -\frac{e}{\epsilon_0} \int_D \int_v f(\vec{r}, \vec{v}, t) d\vec{v} \Psi_l^m = -\frac{e}{\epsilon_0} \int_D \sum_i N_i \delta(\vec{r} - \vec{r}_i) \Psi_l^m \\ &= -\frac{e}{\epsilon_0} \sum_i N_i \Psi_l^m(\vec{r}_i).\end{aligned}\tag{15}$$

In practice, since the basis functions Ψ_l^m have a compact support on mesh cells, only $(m+1)^n$ basis functions need to be evaluated for each macro particle i . The source term is therefore calculated by looping through all the macro particles and accumulating their contribution to the $(m+1)^n$ elements λ_l for which $\Psi_l^m(\vec{r}_i)$ is non-zero.

3.4. Boundaries and boundary conditions definitions

With the web-spline method, Dirichlet boundary conditions are imposed by defining the weight function $w(x)$ and the value at the boundary is set with the function $\tilde{g}(x)$. There is a freedom in defining $w(x)$ and $\tilde{g}(x)$. Within this section, two main methods will be described to create these functions, that are both systematic and robust. Moreover, a 2D domain is considered, but this method can also be applied to 3D. The first method used to define w , that sets the simulation domain D , is based on analytical geometric functions w_i that define elementary geometric shapes. These functions can define, for example, a half-plane, a disc, or a square. One such geometric function w_1 can be the equation delimiting the inside of an ellipse of minor radius a , major radius b and center (x_0, y_0)

$$w_1(x, y) = 1 - \left(\frac{x - x_0}{a} \right)^2 - \left(\frac{y - y_0}{b} \right)^2.\tag{16}$$

These elementary weight functions can be combined by using Rvachev functions to define the union, intersection, or complementary of these elementary domains [37]. The union (+) and intersection (-) of two weights w_1 and w_2 can be calculated with

$$w(x, y) = w_1(x, y) + w_2(x, y) \pm \sqrt{w_1^2(x, y) + w_2^2(x, y)}.\tag{17}$$

Similarly, the complementary of a domain D is defined by taking the negative of the weight function. This method is used in Sec.4.1 to combine two elliptical domains of different major and minor radii and of different center. For this

type of weight, the function \tilde{g} used to impose the Dirichlet boundary conditions can be defined using transfinite interpolation of the potentials g_i imposed on n_i boundaries ∂D_i and defined using weights w_i [38]. In this case:

$$\tilde{g} = \sum_{i=1}^{n_i} g_i \frac{\prod_{j=1; j \neq i}^{n_i} w_j}{\sum_{k=1}^{n_i} \prod_{j=1; j \neq k}^{n_i} w_j}. \quad (18)$$

This function ensures that $\forall \vec{x} \in \partial D_i; g(\vec{x}) = g_i$. Furthermore, if all w_i are continuous, then \tilde{g} is also continuous and that is needed for the stability and physicality of the solution.

The second method to define a boundary is to use spline curves defined using a set of control points, called "knots", in 2D or 3D. The total weight function w , induced by the boundaries ∂D_i can be computed, in this case, using a smoothed distance function to the curves, blended with a plateau of value 1 inside the domain.

$$w = 1 - \sum_{i=1}^{n_i} \max(d_0 - d(x, y; \partial D_i)/d_0, 0)^3, \quad (19)$$

where $d(x, y; \partial D_i)$ is the shortest distance between the point (x, y) and a point on the boundary ∂D_i , and d_0 is the characteristic fall length from the plateau to 0. This variable d_0 is an input parameter and needs to be chosen such that the shortest distance between two boundaries is always greater than d_0 ($d(\partial D_i; \partial D_j) > d_0$). With this method, $w = 1$ on almost all D and $w < 1$ only at a distance $d < d_0$ of the boundaries. This is useful to ensure that at each position in the domain, only one distance function needs to be calculated. This limits the number of calls to the distance function, as this evaluation is numerically expensive and needs to be computed for each macro-particle. The cubic power in w ensures the C^2 -continuity of the weight at the plateau boundary. For this type of boundary conditions, since at most one boundary affects the weight in any position, \tilde{g} can be defined using

$$\tilde{g} = \sum_{i=1}^{n_i} g_i \max(d_0 - d(x, y; \partial D_i)/d_0, 0)^3. \quad (20)$$

Since by the choice of d_0 , only one boundary ∂D_i can be at a distance smaller than d_0 anywhere, the relevant boundary i can be pre-computed in each grid cell during the initialization of the geometry and at most one distance must be computed anywhere. Furthermore, for points sufficiently inside the domain, $w = 1$ and $\tilde{g} = 0$, which is equivalent to the classic b-spline FEM. This greatly reduces the execution time of the code.

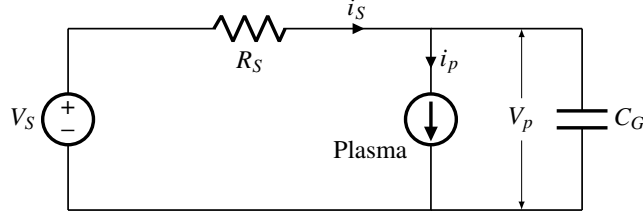


Figure 4: Circuit considered to simulate the effect of a non ideal power supply imposing the external bias between the electrodes.

To impose natural boundary conditions, only the integration domain D needs to be adapted as the FEM ensures by construction $\nabla_{\perp k} \phi = 0$ on ∂D_k . To define D , the current solution is to consider another weight function $w_N(\vec{x}) = 0 \forall \vec{x} \in \partial D_k$ which is used to calculate on each grid-cell, and in each direction, the integration boundaries of D , by finding the roots of w_N . In its current form, FENNECS permits only the definition of Neumann boundary conditions with $\nabla_{\perp k} \phi = 0$ on ∂D_k . However, the web-spline method is more general and the code could be modified with limited effort to include more general Neumann boundary conditions. For the case $\nabla_{\perp k} \phi = g_k$ on ∂D_k , this boundary condition can be imposed by adding a term $\sum_k \int_{\partial D_k} g_k \Psi_l^m$ to λ_l in equation (10).

3.5. Non-Ideal power supply

In addition to constant bias imposed on each electrodes of the domain, the code can simulate the effect of a non-ideal power supplies (PS) imposing the confining biases between two selected electrodes. The PS and load circuit in this case is approximated by the circuit of Figure 4. The power supply is configured to impose a set voltage V_S supposed to be constant in time, and has an internal resistance R_S . The plasma cloud is simulated as a current source generating a current i_p . In addition the capacitive effects of the geometry and of the cables connecting the PS and the electrodes is simulated by a capacitor with capacitance C_G connected in parallel with the plasma cloud. This configuration imposes a bias V_p between the electrodes and is included in the code by changing in time the values g_j corresponding to the boundaries j connected to the PS. The ordinary differential equation of this circuit for the potential V_p is

$$\frac{dV_p(t)}{dt} = \frac{V_S - R_S i_p(t) - V_p(t)}{R_S C_G}. \quad (21)$$

The applied bias V_p is advanced in time using a 4th order Runge-Kutta method every N_s time-steps of the particle advance, by assuming that $i_p(t)$ is only function of time. Here, N_s is an input parameter. The plasma current $i_p(t)$ is measured every $N_s/2$ time steps, by accumulating the charge $q(t_i)$ collected at each time step t_i on the electrodes, giving:

$$i_p(t_{i+N_s/2}) = \frac{1}{\Delta t N_s/2} \sum_{j=i}^{i+N_s/2} q(t_j). \quad (22)$$

Here, Δt is the numerical timestep used to evolve the particles position. Since the PS has a fixed characteristic response time, independent on p_n , and due to the artificial reduction of the time-scale separation defined by the parameter α , the time response of the PS must be rescaled in the simulation. Similarly, as the collected current is linearly proportional to the neutral gas density [9, 26], i_p must be adapted in the simulations. This is particularly important if simulations need to be run for experimental cases in high and ultra high vacuum. To this end the value of R_S is rescaled in the simulations defining $R_{S,\text{simu}} = R_{S,\text{phys}}/\alpha$. This has the effect of rescaling both the power supply time-scales $\tau_{PS} = R_S C_G$, and is equivalent to rescaling the numerical current $i_{p,\text{simu}}(t)$ by $1/\alpha$ due to the term $R_S i_p(t)$ in the differential equation.

3.6. Electron-neutral collisions

The electron-neutral collisions are simulated using a standard Monte Carlo approach [39]. For this process, each macro-particle is temporarily treated as a single particle of the simulated species. At each time step, the collision cross-sections σ_{io} and σ_{ela} are evaluated, from tabulated data [28, 40], for each type of interaction and each macro-particle. For each particle i , a random number $x_{i,1} \in [0, 1]$ is generated according to a uniform distribution function and is used to determine if the particle i of kinetic energy E_i and velocity v_i undergoes a collision event.

1. If $x_{i,1} < 1 - \exp(-n_n(\sigma_{\text{io}}(E_i) + \sigma_{\text{ela}}(E_i))v_i\Delta t)$, with Δt the time step, a collision is triggered.
2. The type of collision is determined using a new random variable $x_{i,2}$. If

$$x_{i,2} < \frac{\sigma_{\text{ela}}(E_i)}{\sigma_{\text{io}}(E_i) + \sigma_{\text{ela}}(E_i)}, \quad (23)$$

an elastic collision is triggered, otherwise an ionization event takes place.

3. In case of an elastic event, the first scattering angle χ is calculated using a singly differential cross-section for screened Coulomb Collision [29, 41], using a third random number $x_{i,3}$, according to

$$\cos(\chi) = 1 - \frac{2x_{i,3}(1 - \xi)}{1 + \xi(1 - 2x_{i,3})}. \quad (24)$$

Here, $\xi = 4E_i/(E_h + 4E_i)$ and $E_h = \hbar^2/(m_e a_0^2) = 27.21\text{eV}$ is one Hartree, the atomic unit of energy, with \hbar the reduced Planck constant and a_0 the Bohr radius. The second scattering angle $\theta = 2\pi x_{i,4}$ is obtained with a fourth random number. The electron velocity is then rotated using χ and θ .

4. In case of an ionization event, the energy splitting between the two resulting electrons is determined using a normalized differential cross-section obtained from experimental data [30] with a random number $x_{i,5}$. The scattered electron kinetic energy E_{sca} is

$$E_{\text{sca}} = E^* \tan(x_{i,5} \arctan((E_i - E_{\text{io}})/(2E^*))), \quad (25)$$

with E^* a fitted scattering factor that depends on the neutral gas [30] and E_{io} the ionization energy of the gas. A new macro-particle is created in the simulation at the position of the particle i and with velocity v_i rescaled such that the kinetic energy of the new particle E_{sec} ensures energy conservation $E_{\text{sec}} = E_i - E_{\text{io}} - E_{\text{sca}}$. The kinetic energy of the incoming particle is then also rescaled to E_{sca} .

5. Both scattered and freed electrons undergo a scattering event using the same differential cross-section as for the elastic collision. The same procedure as in point 3 is used for both electrons.

Depending on the physical system being simulated, the generated ion can either be added to a second species and be tracked in the simulation or not simulated. Ignoring the generated ions is justified in cases where the ions are lost rapidly and where ion induced electron emission happens in regions devoid of trapping mechanism. This rapid loss happen when the ions Larmor radius is larger than the dimensions of the vacuum vessel, which is typically the case in gyrotron electron gun simulations.

3.7. Ion induced emission

In simulations with large electrode bias (above 5kV), the ions generated due to an ionization event are accelerated toward the electrodes and gain large energies,

e.g. of the order of several keV. In this regime, their collision with the electrodes can cause ion induced electron emission (IIEE). This process is currently simulated in the code for several types of metallic surfaces and Hydrogen ions. To calculate the electronic yield $\gamma(E_i)$, defined as the average number of electrons released by one impinging ion, two collision regimes are considered depending on the ion kinetic energy E_i . At low kinetic energies, $E_i < 1$ keV, the electrons of the metal are extracted due to the potential energy of the incoming ions [42]. In this case, the yield depends on the ionization energy E_{i0} necessary to form the incoming ion, the Fermi energy ϵ_F and the work function Φ of the metal, but is independent of the ion kinetic energy,

$$\gamma_{pot} \approx \frac{0.2}{\epsilon_F} (0.8E_{i0} - 2\Phi). \quad (26)$$

At large kinetic energies $E_i > 1$ keV, the energy used to free the metallic electron comes from the kinetic energy of the ion and the yield is calculated using a model derived by Schou [43]

$$\gamma_{kin}(E_i) = \Lambda\beta \left(\frac{dE}{dx} \right)_e. \quad (27)$$

Here, Λ is a material constant, β is a coefficient that accounts for energy transport by recoiling electrons and by backscattered ions, and $\left(\frac{dE}{dx} \right)_e$ is the inelastic stopping power of the impacting ion which depends on the ion type and kinetic energy, and on the material type. As the code currently only considers IIEE by Hydrogen atoms, an experimental parameter $\Lambda\beta = \Lambda_{exp} \approx 0.1 \text{ \AA eV}^{-1}$ is used, which is independent on the metal type [43, 44]. The inelastic stopping power is taken from tabulated data based on experimental data and theoretical predictions [45, 46]. As both types of collision events can happen in the same simulation, the two yields are blended in the range $0 \leq E_i \leq 1$ keV using a linear interpolation between γ_{pot} and $\gamma_{kin}(1 \text{ keV})$ as seen in Figure 5.

To simulate IIEE in the code, the ions generated by electron-neutral collisions are simulated and tracked. Once an ion reaches an electrode, its kinetic energy E_i and yield $\gamma(E_i)$ are calculated. To determine the number of macro-electrons generated, a random number k is generated according to a Poisson distribution with mean $\langle k \rangle = \gamma(E_i)$ such that the probability of freeing k electrons is

$$P(k) = \frac{\exp(-\gamma(E_i))}{k!}. \quad (28)$$

k macro-electrons are then generated at the last known position of the ion inside the domain. The k resulting electrons are given a velocity normal to the electrode

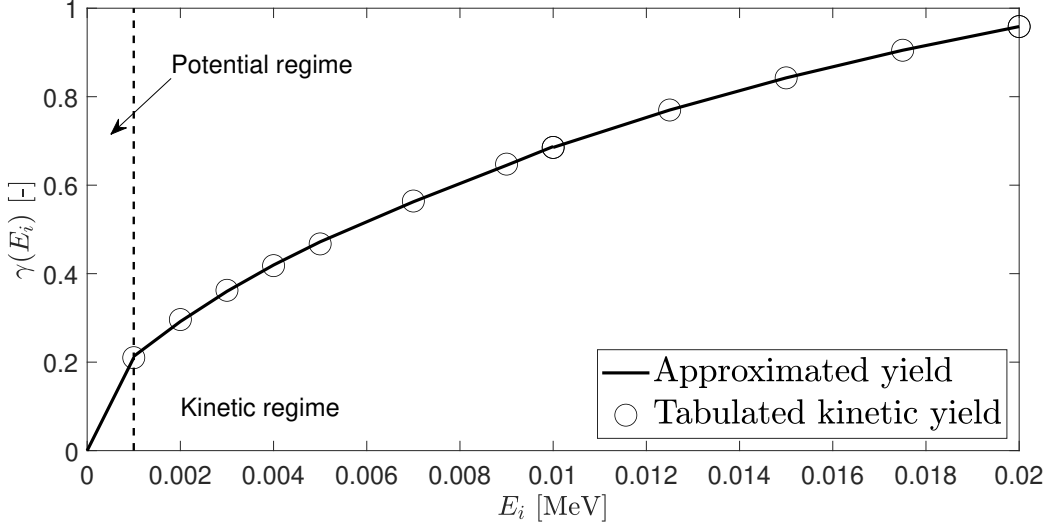


Figure 5: IIEE yield used in FENNECS for Hydrogen atoms hitting aluminum electrodes as a function of the incoming ion kinetic energy. The circles show the effective yield calculated using (27) and tabulated inelastic stopping power [45, 46]. For this electrode material $\gamma_{pot} = 0$.

surface. To simulate the emitted electron energy spectra [43], the kinetic energy of the generated electrons E_e is given using a gamma distribution function which best fits experimental measurements [47]. We recall here the probability density function of the gamma distribution with parameters κ and θ and mean $\langle x \rangle = \kappa\theta$:

$$f_\gamma(x) = \frac{1}{\Gamma(\kappa)\theta^\kappa} x^{\kappa-1} \exp\left(-\frac{x}{\theta}\right). \quad (29)$$

Here $\Gamma(\kappa)$ is the gamma function

$$\Gamma(\kappa) = \int_0^\infty t^{\kappa-1} e^{-t} dt. \quad (30)$$

As a first approximation, the parameters $\kappa = 4$ and $\theta = 0.5$ of the distribution function are independent of the electrode material and impose a mean kinetic energy of the generated electrons $\langle E_e \rangle = 2$ eV. This approximation is supported by the fact that, in gyrotron gun simulations, large electric fields are externally imposed, and the initial electron kinetic energy becomes negligible compared to the one gained by electric field acceleration.

3.8. Seed sources

In addition to the electron sources resulting from the ion-induced electron emission and the impact ionization of the neutrals, a volumetric seed source is

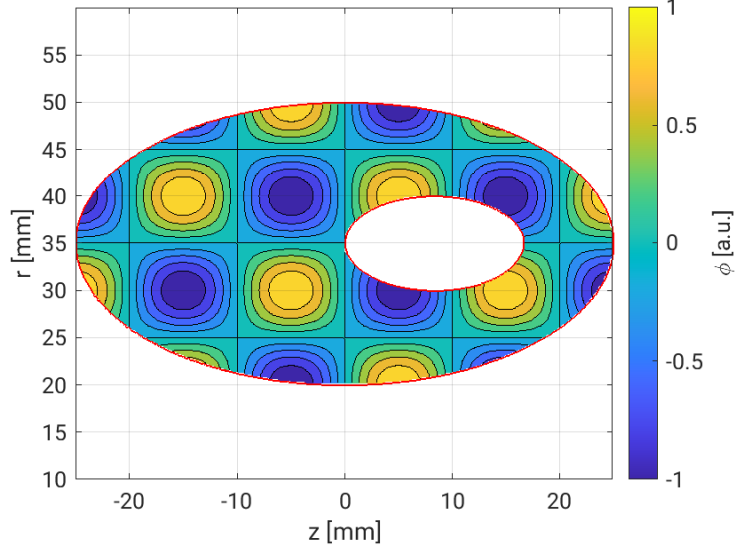


Figure 6: Domain and manufactured solution of the potential used to verify the implementation of the FEM solver.

implemented in the code. This source can generate electrons in a fixed volume according to various types of distribution functions in velocity. For example, a Maxwellian distribution function with temperature T or a mono-velocity beam can be used. The amplitude and spacial distribution of the source is also an input parameter. This source can be used to simulate the effect of neutral ionization due to background radiation, or to simulate the effect of field-emissions on the electrodes. It is sometimes necessary to ensure that some electrons are present at all times in the simulation domain and can start the cloud formation cascade [9]. Indeed, without this source, the initial electron cloud population might be entirely lost due to electron-neutral friction drifts and no new electron cloud could be generated.

4. Verifications

To verify the correct implementation of the code, a set of test cases have been run and are presented in this section.

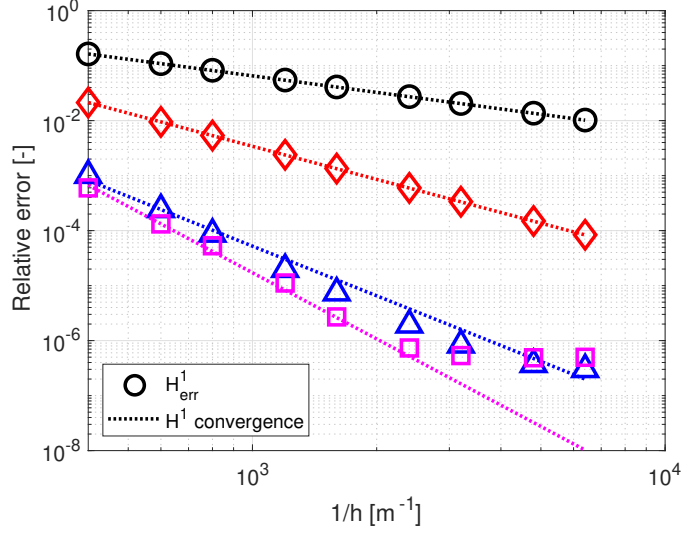


Figure 7: H^1 norm of the relative error for spline orders from 2 to 5 ($\circ, \diamond, \triangle, \square$) and varying grid width h . The dotted line highlights the ideal convergence for each spline order. Each order is color coded (black, red, blue, magenta) for readability.

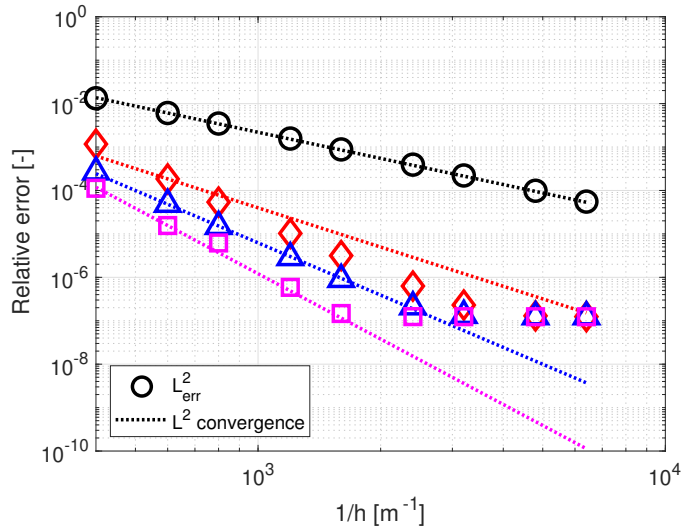


Figure 8: L^2 norm of the relative error for spline orders from 2 to 5 ($\circ, \diamond, \triangle, \square$) and varying grid width h . The dotted line highlights the ideal convergence for each spline order. Each order is color coded (black, red, blue, magenta) for readability.

4.1. General complex geometry Poisson solver

The Poisson solver is verified using a manufactured solution of the form

$$\phi = \sin\left(\pi \frac{z - z_0}{L_z}\right) \sin\left(\pi \frac{r - r_0}{L_r}\right), \quad (31)$$

which satisfies the Poisson equation with the source term:

$$\begin{aligned} Q = & \left(\frac{\pi}{L_z}\right)^2 \sin\left(\pi \frac{z - z_0}{L_z}\right) \sin\left(\pi \frac{r - r_0}{L_r}\right) \\ & + \frac{\pi}{L_r} \sin\left(\pi \frac{z - z_0}{L_z}\right) \left[-\frac{1}{r} \cos\left(\pi \frac{r - r_0}{L_r}\right) \right. \\ & \left. + \frac{\pi}{L_r} \sin\left(\pi \frac{r - r_0}{L_r}\right) \right], \end{aligned} \quad (32)$$

on a domain defined using the Rvachev intersection of two domains defined with ellipses, as represented in Figure 6. The spline grid is defined with $-25 \leq z \leq 25$ mm and $10 \leq r \leq 60$ mm and for an increasing number of grid cells per dimension, from 20 to 320. The manufactured solution parameters are $r_0 = 35$ mm, $z_0 = 0$ mm, $L_r = 10$ mm and $L_z = 10$ mm. The inner ellipse is defined with the geometric weight

$$w_1 = \left(\frac{r - 35}{8.3}\right)^2 - \left(\frac{z - 8.3}{8.3}\right)^2 - 1, \quad (33)$$

and the outer ellipse is defined with

$$w_2 = 1 - \left(\frac{r - 35}{15}\right)^2 - \left(\frac{z}{25}\right)^2. \quad (34)$$

Here r and z are defined in mm. The error in the solution is evaluated using both the L^2 and the H^1 norms defined respectively as

$$e_2 = \|\phi_h - \phi\|_{L^2} = \left(\int_D (\phi_h - \phi)^2 dV \right)^{1/2}, \quad (35)$$

and

$$e_1 = \|\phi_h - \phi\|_{H^1} = \left(\int_D \phi_h - \phi^2 + |\nabla(\phi_h - \phi)|^2 dV \right)^{1/2}. \quad (36)$$

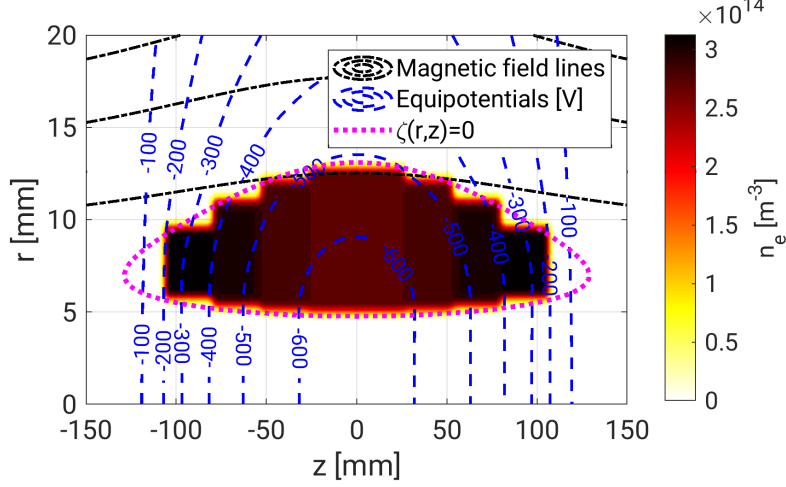


Figure 9: Zoom on the initial density loading of the electron cloud and steady-state $\zeta = 0$ contour (dotted magenta). In addition, the electric equipotential (dashed blue) and magnetic field lines (dash-dotted black) are represented.

It can be shown [35] that $e_1 \sim O(h^{m-1})$ as $h \rightarrow 0$ when using web-splines of order m . Similarly, it can be shown that $e_2 \sim O(h^m)$ as $h \rightarrow 0$ when using web-splines of order m . Evaluations of the relative error using the H^1 and L^2 norms are represented in Figure 7 and Figure 8 using the manufactured solution previously defined. We observed the correct convergence rates for different orders of the web-spline basis until they reach a plateau for a relative accuracy close to 10^{-7} . We think this plateau is due to the large condition number of the matrices for very small values of the grid width h . We have not investigated this point further, as the achieved accuracy is well beyond the accuracy of other components of the PIC algorithm. This plateau observed at high accuracy for the Poisson solver will not affect the overall accuracy of FENNECS.

4.2. Equilibrium of a ring of charges trapped in a magnetic mirror

In this section we present the results of simulations of a pure electron plasma equilibrium for which an analytical solution exists. This particular Vlasov electrostatic equilibrium considers an annular electron cloud trapped radially by a strong magnetic field and trapped axially by a magnetic mirror of length L [2, 48]. The magnetic vector potential for an externally imposed mirror field is described ana-

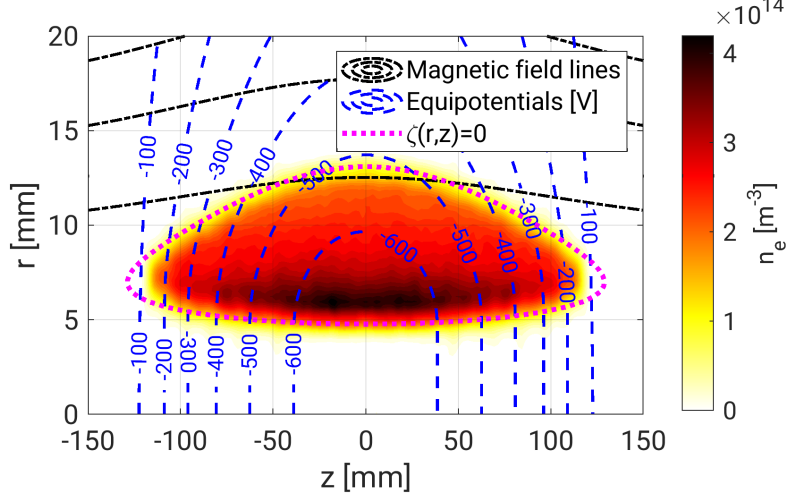


Figure 10: Zoom on the final density of the electron cloud and steady-state $\zeta = 0$ contour (dotted magenta). In addition, the electric equipotential (dashed blue) and magnetic field lines (dash-dotted black) are represented.

lytically by

$$A_0^{\text{ext}}(r, z) = \frac{1}{2} B_0 \left[r - \left(\frac{L}{\pi} \frac{R-1}{R+1} \right) I_1 \left(\frac{2\pi r}{L} \right) \cos \left(\frac{2\pi z}{L} \right) \right], \quad (37)$$

with B_0 the magnetic field amplitude on axis at $z = \pm L/4$, I_1 the modified Bessel function of order one, L the distance between the mirror coils, and R the mirror ratio defined by $R \equiv B_{\text{max}}/B_{\text{min}} = B_0^{\text{ext}}(r=0, z=\pm L/2)/B_0^{\text{ext}}(r=0, z=0)$. The distribution function is written in terms of conserved quantities, namely the total energy $H = p^2/(2m_e) - e\phi(r, z)$, with $\vec{p} = m_e \vec{v}$, and the canonical angular momentum $P_\theta = r[p_\theta - eA_0^{\text{ext}}(r, z)]$,

$$f_e(H, P_\theta) = \frac{n_0 R_0}{2\pi m_e} \delta(H - H_0) \delta(P_\theta - P_0). \quad (38)$$

Here, n_0 is the maximum electron density in the cloud, R_0 is the lower radial limit of the cloud at $z = 0$, H_0 and P_0 are positive constants, and p_θ is the electron momentum in the azimuthal direction. Equation (38) is a solution of the Vlasov equation. For this equilibrium, one can show that an envelope function $\zeta(r, z)$ can be defined [48]:

$$\zeta(r, z) = \frac{p_\perp^2(r, z)}{2m_e H_0} = 1 + \frac{e\phi}{H_0} - \frac{1}{2m_e H_0} \left[\frac{P_0}{r} + eA_0^{\text{ext}} \right]^2, \quad (39)$$

B_0	0.21 T
R	1.5
$L = L_z$	0.48 m
r_b	0.06 m
Δz	1.9×10^{-3} m
Δr	2.8×10^{-4} m
Δt	5×10^{-12} s $\approx 0.2 m_e / e B_0$
n_0	5×10^{14} m $^{-3}$
R_0	0.005 m
H_0	3.2×10^{-14} J
P_0	8.66×10^{-26} kg m 2 s $^{-1}$

Table 1: Physical and numerical parameters used in the simulation of the annular electron cloud trapped in a magnetic mirror.

such that the curve where $\zeta(r, z) = 0$ denotes the limit of the electron cloud. Here, p_\perp is the momentum perpendicular to the magnetic field line and ϕ is the self-consistent electric potential. The electron density is therefore:

$$n_e(r, z) = \frac{R_0}{r} n_0 U[\zeta(r, z)], \quad (40)$$

with $U[x]$ the Heaviside step function. To verify the code implementation, a cloud of electrons is loaded in FENNECS with $H_0 = 3.2 \times 10^{-14}$ J and $P_0 = 8.66 \times 10^{-26}$ kg m 2 s $^{-1}$ in the region where $\zeta_0 = 1 - \frac{1}{2m_e H_0} \left[\frac{P_0}{r} + e A_0^{\text{ext}} \right]^2 > 0$ using a uniform density distribution function as seen in Figure 9. The number of loaded macro particles is 2116800 with a macro particle weight $w_p = 1.018 \cdot 10^4$ such that the reference density in steady state is $n_0 = 5 \times 10^{14}$ m $^{-3}$. The simulation domain is defined with a cylindrical volume of radius r_b and length L_z as shown in Figure 9. The volume is enclosed radially by a cylindrical conductor of radius r_b at ground. The system and numerical parameters are given in Table 1.

The simulation is run with a timestep $\Delta t = 5 \times 10^{-12}$ s $\approx 0.2 / \Omega_{ce}$ and the total kinetic and potential energies of the cloud are monitored. As shown in Figure 11, the total energy summed over all particles E_{tot} is conserved on average and the relative error on the energy is kept below 10^{-4} over long time scales as compared to the bounce time of electrons. During the simulation no particles are lost, and after a time $t = 364$ ns $\approx 460 / \omega_{pe}$, the system is in a steady state and successfully retrieves the analytical solution of the equilibrium. In particular, the $1/r$ radial dependency of the electron cloud density, as predicted by equation (40), is well

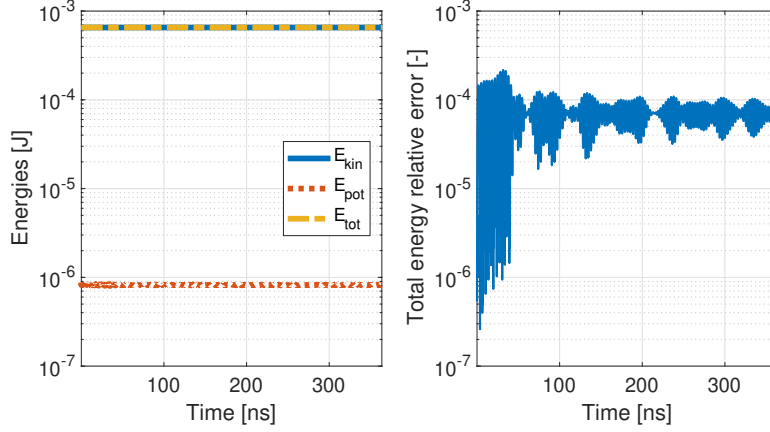


Figure 11: Left: Time evolution of the total (yellow), kinetic (blue) and potential (red) energies during the simulation. Right: Relative error on the total energy conservation during the simulation.

reproduced and the cloud remains limited by the envelope function as can be observed in Figure 10 and Figure 12.

4.3. Radial drifts due to collisions

To verify the electron neutral collision implementation, an annular electron cloud is considered in a coaxial configuration of infinite length, subjected to a uniform axial magnetic field, and to elastic collisions with a residual neutral gas. We assume that the distribution remains close to isotropic and study the system using a fluid model [9]. In this model the force balance equation is

$$n_e m_e \frac{d\vec{u}}{dt} = -n_e e \left(\vec{E} + \vec{u} \times \vec{B} \right) - n_e m_e \nu_{\text{ela,mom}} \vec{u} - \nabla P. \quad (41)$$

Here, \vec{u} is the fluid velocity of the electrons, n_e is the local electron density, $\nu_{\text{ela,mom}} = n_n \langle \int \frac{d\sigma_{\text{ela}}}{d\Omega} v d\Omega \rangle_f$ is the averaged collision frequency for momentum exchange, $\langle \rangle_f$ denotes the average over the distribution function, and P is the pressure. Due to the azimuthal symmetry considered, the pressure term is identically 0 in the azimuthal direction. Neglecting all inertial terms, equation (41) in the azimuthal direction gives the radial electron flux $\Gamma_r(r) = n_e u_r$ caused by the collisional drag:

$$\Gamma_r(r) = -n_e \frac{u_\theta \nu_{\text{ela,mom}}}{\Omega_c}. \quad (42)$$

In the simulations, the system is defined with a coaxial configuration of infinite length, using periodic boundary conditions for the particles and natural boundary

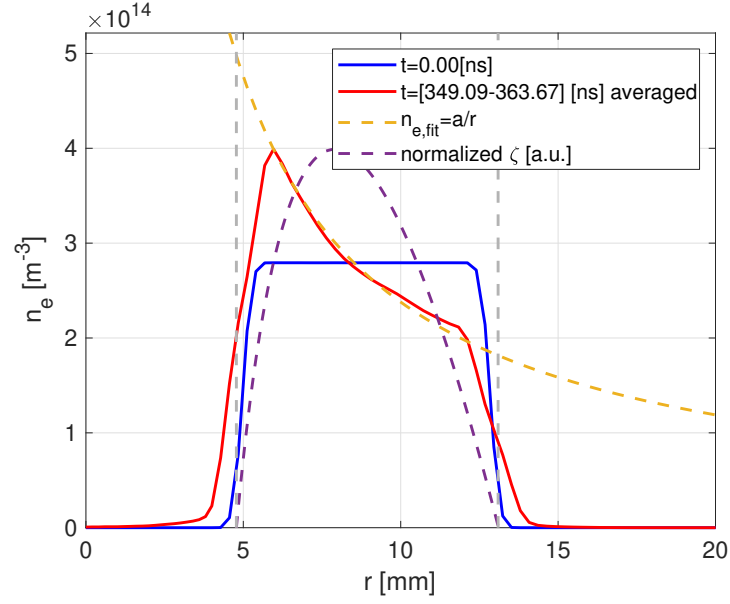


Figure 12: Initial (solid blue) and steady-state (solid red) radial density profile at $z = 0$, $1/r$ fit of the steady-state density profile (dashed yellow) and normalized ζ (dashed purple) at the same axial position. The vertical gray dashed lines highlight the radial positions for which $\zeta = 0$.

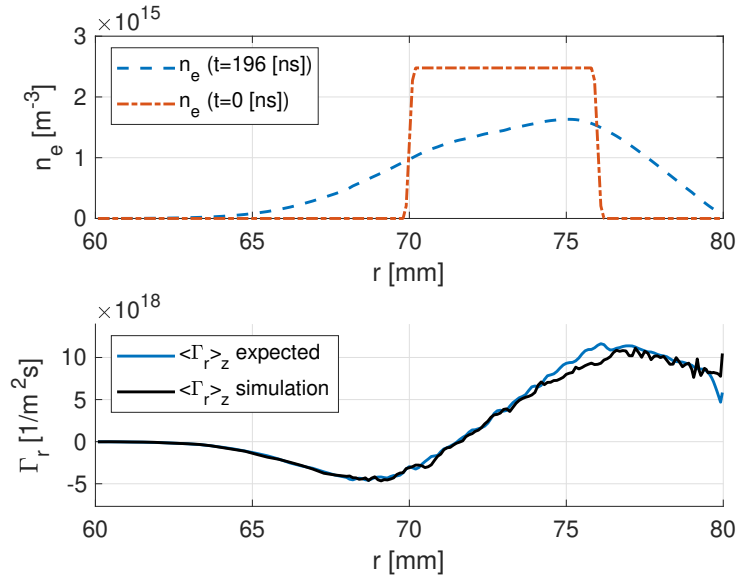


Figure 13: Top: initial and final radial electron density profile. Bottom: Expected (blue) and simulated (black) radial flux at the end of the simulation.

conditions for the fields. A bias $\Delta\phi = 300\text{ V}$ is applied between the electrodes and the system is also subjected to a uniform external magnetic field of amplitude $B_0 = 0.28\text{ T}$. In this configuration, a cloud of uniform density $n_e^0 = 2.5 \times 10^{15}\text{ m}^{-3}$ and uniform velocity, as represented in Figure 13 is loaded on an annulus between $r = 70\text{ mm}$ and $r = 76\text{ mm}$. The simulation is set with periodic axial boundary conditions for the particles to simulate the infinite length and is run for several elastic collision characteristic times. The simulation results show indeed that the distribution function remains isotropic and that the inertial terms are small compared to the Lorentz and collisional drag terms. The radial flux is measured in the code and compared to the prediction obtained using the cold fluid model (42). The fluid azimuthal velocity is extracted from the code, and the averaged collision frequency is evaluated with the final electron distribution function extracted from the simulation results. Both the expected and simulated fluxes are averaged along the axial direction to reduce the numerical noise. As shown in Figure 13, both fluxes exhibit the same behavior throughout the simulation domain with a maximum relative error of 20% at $r = 76\text{ mm}$.

4.4. Ion induced emission

The IIEE module is verified with a coaxial configuration with an inner electrode at $r_a = 1\text{ mm}$ and an outer electrode at $r_b = 10\text{ mm}$ with an axial uniform magnetic field of amplitude $B_0 = 0.21\text{ T}$. A bias $\Delta\phi = 20\text{ kV}$ is imposed between the electrodes and three clouds of 1000 Hydrogen ions each are loaded at different radial positions $r_1 = 3\text{ mm}$, $r_2 = 5\text{ mm}$ and $r_3 = 8\text{ mm}$ with zero velocity. In this configuration, the ions are accelerated radially towards the central electrode, gaining a kinetic energy $E_{kin}(r_j) \equiv E_j = e(\phi(r_j) - \phi(r_a))$ that depends on their initial radial position r_j . The effective yield obtained in the simulation is then compared to the theoretical yield $\gamma_{kin}(E_j)$ for each initial position r_j . The results of these simulations are given for three electrode materials in Table 2, and show an agreement between the theoretical yields γ_{exp} and simulation yields γ_{sim} within 2%.

5. Parallel performance

The code is parallelized using a hybrid OpenMP/MPI approach. Indeed, the code is first parallelized using MPI and a non-uniform axial domain decomposition. This choice is supported by the fact that the particle distribution is usually not uniform axially, as illustrated by the test case described in Sec.4.2. Thus, to

Material	³⁰⁴ SS	r_1	r_2	r_3
	γ_{exp}	1.311	1.623	1.870
	γ_{sim}	1.299	1.627	1.891
	Rel. error	0.9%	0.2%	1.1%
Material	Cu	r_1	r_2	r_3
	γ_{exp}	1.237	1.522	1.746
	γ_{sim}	1.229	1.518	1.760
	Rel. error	0.6%	0.3%	0.8%
Material	Al	r_1	r_2	r_3
	γ_{exp}	0.920	1.133	1.297
	γ_{sim}	0.910	1.115	1.293
	Rel. error	1.0%	1.6%	0.3%

Table 2: Expected and simulation yield obtained for the IIEE verification case considering: stainless steel 304, copper and aluminum as electrode material, and 3 initial radial position of the ions.

ensure a good load balancing for the computation of the particle trajectories between each task, the axial length covered by each task must be different. On each node, OpenMP parallelism is used to parallelize the computation of the particle trajectories. The Poisson solver is currently using the MUMPS library in serial mode, but the solver could, in principle, be adapted to leverage the OpenMP and MPI parallelism. Strong scaling studies have been run on the jed cluster of EPFL using an increasing number of tasks and 4 threads per task as shown in Figure 14. For this study, we considered a coaxial geometry in which 10 million particles are simulated on a (100x156) grid. The strong scaling results show a parallel efficiency above 90% for up to 4 tasks with each 4 OpenMP threads corresponding to a total of 16 CPUs. The parallel efficiency η_{par} is defined as the ratio between the time t_1 to run the task with a given number of cores, and N times t_N the time needed to run when N times more cores are used ($\eta_{par} = t_1 / (N t_N)$).

6. Summary and conclusions

The present paper describes the code FENNECS solving the Boltzmann-Poisson equations for a non-neutral plasma subject to strong electric fields generated by electrodes of complex shapes and space-charge effects, and to strong external magnetic fields. The novel numerical method used to simulate the complex electrode geometries present in gyrotron electron guns is also described. The different electron sources considered in the code are presented. More specifically,

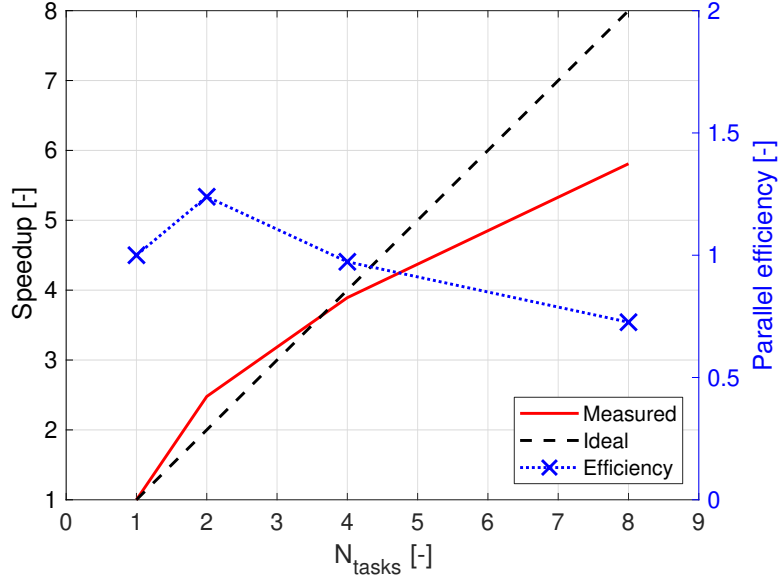


Figure 14: Strong scaling and parallel efficiency of FENNECS for a case considering 10M macro-particles in a coaxial geometry. Each task is set to use 4 OpenMP threads.

the Monte Carlo method used to simulate the electron-neutral collisions (elastic and ionization), and the emission of electrons at the electrode surfaces due to collisions of energetic ions on the electrode surfaces are also described. A set of verification cases are presented and confirm the correct implementation of the governing equations. In addition, the cases underline the efficiency of the novel web-spline method and demonstrate its capability of reaching arbitrary precision for the electrostatic potential.

The code is parallelized using a hybrid OpenMP/MPI approach allowing to leverage the capabilities of modern computers and computational clusters. Scalability studies have shown a reasonable speed-up of the code for workstations and small cluster use. This allows the code to be used for parametric studies and to guide the design of electron guns.

FENNECS has already been used to study trapped electron clouds in existing gyrotron electron guns [9, 26] and has shown its relevance as a design tool for future gyrotron electron gun. It has also been used to support the design of the T-REX experiment [49] and to define the relevant diagnostics and geometries to study the problem of trapped electron clouds in a more controlled environment. Furthermore, the authors believe that the governing equations are sufficiently general that the code can also be applied to study arc formations, and more

conventional Penning-Malmberg traps. As the code is open-source, it can easily be adapted to study other problems of plasma physics, where electrode geometric effects are non-negligible.

Acknowledgments

The authors would like to thank Trach-Minh Tran and Patryk Kamiński who developed the initial code `espic2d` on which FENNECS is based, where no geometry effects and no electron-neutral collision effects were considered.

This work has been carried out within the framework of the EUROfusion Consortium, via the Euratom Research and Training Programme (Grant Agreement No 101052200 — EUROfusion) and funded by the Swiss State Secretariat for Education, Research and Innovation (SERI). Views and opinions expressed are however those of the author(s) only and do not necessarily reflect those of the European Union, the European Commission, or SERI. Neither the European Union nor the European Commission nor SERI can be held responsible for them. The calculations have been performed using the facilities of the Scientific IT and Application Support Center of EPFL. This work was supported in part by the Swiss National Science Foundation under grant No. 204631.

Data Availability Statement

The data that support the findings of this study are available from the corresponding author upon reasonable request.

References

- [1] M. Vogel, Particle Confinement in Penning Traps, Vol. 100 of Springer Series on Atomic, Optical, and Plasma Physics, Springer International Publishing, Cham, 2018. doi:10.1007/978-3-319-76264-7.
URL <http://link.springer.com/10.1007/978-3-319-76264-7>
- [2] R. C. Davidson, Physics of Nonneutral Plasmas, CO-PUBLISHED WITH WORLD SCIENTIFIC PUBLISHING CO, 2001. doi:10.1142/p251.
URL <http://www.worldscientific.com/worldscibooks/10.1142/p251>
- [3] K. R. Chu, The electron cyclotron maser, Rev. Mod. Phys. 76 (2) (2004) 489–540, publisher: American Physical Society. doi:10.1103/

RevModPhys.76.489.

URL <https://link.aps.org/doi/10.1103/RevModPhys.76.489>

- [4] T. Mohamed, A. Mohri, Y. Yamazaki, Comparison of non-neutral electron plasma confinement in harmonic and rectangular potentials in a very dense regime, *Physics of Plasmas* 20 (1) (2013) 012502, publisher: American Institute of Physics. doi:10.1063/1.4773900.
URL <https://aip.scitation.org/doi/10.1063/1.4773900>
- [5] W. A. Bertsche, E. Butler, M. Charlton, N. Madsen, Physics with antihydrogen, *Journal of Physics B: Atomic, Molecular and Optical Physics* 48 (23) (2015) 232001, publisher: IOP Publishing. doi:10.1088/0953-4075/48/23/232001.
URL <https://dx.doi.org/10.1088/0953-4075/48/23/232001>
- [6] P. Pérez, D. Banerjee, F. Biraben, D. Brook-Roberge, M. Charlton, P. Cladé, P. Comini, P. Crivelli, O. Dalkarov, P. Debu, A. Douillet, G. Dufour, P. Dupré, S. Eriksson, P. Froelich, P. Grandemange, S. Guellati, R. Guérout, J. M. Heinrich, P.-A. Hervieux, L. Hilico, A. Husson, P. Indelicato, S. Jones, J.-P. Karr, K. Khabarova, N. Kolachevsky, N. Kuroda, A. Lambrecht, A. M. M. Leite, L. Liskay, D. Lunney, N. Madsen, G. Manfredi, B. Mansoulié, Y. Matsuda, A. Mohri, T. Mortensen, Y. Nagashima, V. Nesvizhevsky, F. Nez, C. Regenfus, J.-M. Rey, J.-M. Raymond, S. Reynaud, A. Rubbia, Y. Sacquin, F. Schmidt-Kaler, N. Sillitoe, M. Staszczak, C. I. Szabo-Foster, H. Torii, B. Vallage, M. Valdes, D. P. Van der Werf, A. Voronin, J. Walz, S. Wolf, S. Wronka, Y. Yamazaki, The GBAR antimatter gravity experiment, *Hyperfine Interactions* 233 (1) (2015) 21–27. doi:10.1007/s10751-015-1154-8.
URL <https://doi.org/10.1007/s10751-015-1154-8>
- [7] M. R. Stoneking, T. S. Pedersen, P. Helander, H. Chen, U. Hergenhahn, E. V. Stenson, G. Fiksel, J. v. d. Linden, H. Saitoh, C. M. Surko, J. R. Danielson, C. Hugenschmidt, J. Horn-Stanja, A. Mishchenko, D. Kennedy, A. Deller, A. Card, S. Nißl, M. Singer, S. König, L. Willingale, J. Peebles, M. R. Edwards, K. Chin, A new frontier in laboratory physics: magnetized electron-positron plasmas, *Journal of Plasma Physics* 86 (6) (2020) 155860601, publisher: Cambridge University Press. doi:10.1017/S0022377820001385.
URL <https://www.cambridge.org/core/>

journals/journal-of-plasma-physics/article/
new-frontier-in-laboratory-physics-magnetized-electronpositron-plasmas/
F86C1C197E256296EE9C86045C692FD7

- [8] I. G. Pagonakis, J. Hogge, T. Goodman, S. Alberti, B. Piosczyk, S. Illy, T. Rzesnicki, S. Kern, C. Lievin, Gun design criteria for the refurbishment of the first prototype of the EU 170GHz/2MW/CW coaxial cavity gyrotron for ITER, in: 2009 34th International Conference on Infrared, Millimeter, and Terahertz Waves, 2009, pp. 1–2. doi:10.1109/ICIMW.2009.5324625.
- [9] G. Le Bars, J.-P. Hogge, J. Loizu, S. Alberti, F. Romano, A. Cerfon, Self-consistent formation and steady-state characterization of trapped high-energy electron clouds in the presence of a neutral gas background, *Physics of Plasmas* 29 (8) (2022) 082105, publisher: American Institute of Physics. doi:10.1063/5.0098567.
URL <https://aip.scitation.org/doi/full/10.1063/5.0098567>
- [10] I. G. Pagonakis, B. Piosczyk, J. Zhang, S. Illy, T. Rzesnicki, J.-P. Hogge, K. Avramidis, G. Gantenbein, M. Thumm, J. Jelonnek, Electron trapping mechanisms in magnetron injection guns, *Physics of Plasmas* 23 (2) (2016) 023105. doi:10.1063/1.4941705.
URL <https://aip.scitation.org/doi/abs/10.1063/1.4941705>
- [11] LSP Suite.
URL <https://www.northropgrumman.com/space/pic-code-software/lsp-suite>
- [12] A. J. Woods, L. D. Ludeking, MAGIC electromagnetic FDTD-PIC code dense plasma model comparison with Lsp, in: 2009 IEEE International Vacuum Electronics Conference, 2009, pp. 165–166. doi:10.1109/IVELEC.2009.5193488.
- [13] S. Mattei, K. Nishida, M. Onai, J. Lettry, M. Q. Tran, A. Hatayama, A fully-implicit Particle-In-Cell Monte Carlo Collision code for the simulation of inductively coupled plasmas, *Journal of Computational Physics* 350 (2017) 891–906. doi:10.1016/j.jcp.2017.09.015.
URL <https://www.sciencedirect.com/science/article/pii/S0021999117306745>
- [14] B. Herrmannsfeldt, ELECTRON TRAJECTORY PROGRAM.

- [15] S. Illy, J. Zhang, J. Jelonnek, Gyrotron electron gun and collector simulation with the ESRAY beam optics code, in: 2015 IEEE International Vacuum Electronics Conference (IVEC), 2015, pp. 1–2. doi:10.1109/IVEC.2015.7223779.
- [16] L. S. C. d. R. e. P. d. P. C. Ecole Polytechnique Federale, Papers presented at the 6 joint EPS-APS international conference on physics computing, Tech. rep., Switzerland, IRP-494/94 INIS Reference Number: 25050357 (1994).
- [17] I. G. Pagonakis, J. L. Vomvoridis, The self-consistent 3D trajectory electrostatic code ARIADNE for gyrotron beam tunnel simulation, in: Infrared and Millimeter Waves, Conference Digest of the 2004 Joint 29th International Conference on 2004 and 12th International Conference on Terahertz Electronics, 2004., 2004, pp. 657–658. doi:10.1109/ICIMW.2004.1422262.
- [18] D. P. Grote, A. Friedman, J. Vay, I. Haber, The WARP Code: Modeling High Intensity Ion Beams, AIP Conference Proceedings 749 (1) (2005) 55–58, publisher: American Institute of Physics. doi:10.1063/1.1893366. URL <https://aip.scitation.org/doi/abs/10.1063/1.1893366>
- [19] J.-L. Vay, D. Grote, R. Cohen, A. Friedman, Novel methods in the Particle-In-Cell accelerator Code-Framework Warp, Computational Science & Discovery 5 (2012) 014019. doi:10.1088/1749-4699/5/1/014019.
- [20] A. Friedman, R. H. Cohen, D. P. Grote, S. M. Lund, W. M. Sharp, J.-L. Vay, I. Haber, R. A. Kishek, Computational Methods in the Warp Code Framework for Kinetic Simulations of Particle Beams and Plasmas, IEEE Transactions on Plasma Science 42 (5) (2014) 1321–1334, conference Name: IEEE Transactions on Plasma Science. doi:10.1109/TPS.2014.2308546.
- [21] K. Höllig, C. Apprich, A. Streit, Introduction to the Web-method and its applications, Advances in Computational Mathematics 23 (1) (2005) 215–237. doi:10.1007/s10444-004-1811-y. URL <https://doi.org/10.1007/s10444-004-1811-y>
- [22] G. Apaydin, N. Ari, Use of WEB-splines of arbitrary domain for waveguides, in: 2008 12th International Conference on Mathematical Methods in Electromagnetic Theory, 2008, pp. 385–388, iSSN: 2161-1750. doi:10.1109/MMET.2008.4581003.

- [23] V. V. K. S. Kumar, B. V. R. Kumar, P. C. Das, Weighted extended B-spline method for the approximation of the stationary Stokes problem, *Journal of Computational and Applied Mathematics* 186 (2) (2006) 335–348. doi:10.1016/j.cam.2005.02.008.
URL <https://www.sciencedirect.com/science/article/pii/S0377042705000981>
- [24] K. Höllig, U. Reif, J. Wipper, Weighted Extended B-Spline Approximation of Dirichlet Problems, *SIAM Journal on Numerical Analysis* 39 (2) (2001) 442–462, publisher: Society for Industrial and Applied Mathematics. doi:10.1137/S0036142900373208.
URL <https://epubs.siam.org/doi/abs/10.1137/S0036142900373208>
- [25] K. Höllig, *Finite Element Methods with B-Splines*, *Frontiers in Applied Mathematics*, Society for Industrial and Applied Mathematics, 2003. doi:10.1137/1.9780898717532.
URL <https://epubs.siam.org/doi/book/10.1137/1.9780898717532>
- [26] G. Le Bars, J. Loizu, J.-P. Hogge, S. Alberti, F. Romano, J. Genoud, I. Pagonakis, First self-consistent simulations of trapped electron clouds in a gyrotron gun and comparison with experiments, *Physics of Plasmas* 30 (3), publisher: American Institute of Physics (Mar. 2023).
- [27] A. Anders, *Cathodic Arcs: From Fractal Spots to Energetic Condensation*, Springer Science & Business Media, 2009, google-Books-ID: rwIUhsbB-HQYC.
- [28] Biagi-v8.9 database, private communication, www.lxcat.net, retrieved on June 1 (Jun. 2021).
- [29] A. Okhrimovskyy, A. Bogaerts, R. Gijbels, Electron anisotropic scattering in gases: A formula for Monte Carlo simulations, *Physical Review E* 65 (3) (2002) 037402, publisher: American Physical Society. doi:10.1103/PhysRevE.65.037402.
URL <https://link.aps.org/doi/10.1103/PhysRevE.65.037402>
- [30] C. B. Opal, W. K. Peterson, E. C. Beaty, Measurements of Secondary-Electron Spectra Produced by Electron Impact Ionization of a Number of

- Simple Gases, *The Journal of Chemical Physics* 55 (8) (1971) 4100–4106, publisher: American Institute of Physics. doi:10.1063/1.1676707.
URL <https://aip.scitation.org/doi/10.1063/1.1676707>
- [31] T. Holstein, Energy Distribution of Electrons in High Frequency Gas Discharges, *Physical Review* 70 (5-6) (1946) 367–384, publisher: American Physical Society. doi:10.1103/PhysRev.70.367.
URL <https://link.aps.org/doi/10.1103/PhysRev.70.367>
- [32] S. Yoshida, A. V. Phelps, L. C. Pitchford, Effect of electrons produced by ionization on calculated electron-energy distributions, *Physical Review A* 27 (6) (1983) 2858–2867, publisher: American Physical Society. doi:10.1103/PhysRevA.27.2858.
URL <https://link.aps.org/doi/10.1103/PhysRevA.27.2858>
- [33] J. P. Boris, others, Relativistic plasma simulation-optimization of a hybrid code, in: *Proc. Fourth Conf. Num. Sim. Plasmas*, 1970, pp. 3–67.
- [34] Ahlberg, J. H., Nilson, Edwin N., Walsh, J. L., *The Theory of Splines and Their Applications*, Academic Press New York, 1967.
URL <https://www.elsevier.com/books/the-theory-of-splines-and-their-applications/ahlberg/978-1-4831-9792-0>
- [35] K. Höllig, J. Hörner, *Approximation and Modeling with B-Splines, Other Titles in Applied Mathematics*, Society for Industrial and Applied Mathematics, 2013. doi:10.1137/1.9781611972955.
URL <https://epubs.siam.org/doi/book/10.1137/1.9781611972955>
- [36] E. T. Y. Lee, Marsden’s identity, *Computer Aided Geometric Design* 13 (4) (1996) 287–305. doi:10.1016/0167-8396(95)00027-5.
URL <https://www.sciencedirect.com/science/article/pii/0167839695000275>
- [37] V. L. Rvachev, Method of R-functions in boundary-value problems, *Soviet Applied Mechanics* 11 (4) (1975) 345–354. doi:10.1007/BF00882900.
URL <https://doi.org/10.1007/BF00882900>
- [38] V. L. Rvachev, T. I. Sheiko, V. Shapiro, I. Tsukanov, Transfinite interpolation over implicitly defined sets, *Computer Aided Geometric Design* 18 (3)

- (2001) 195–220. doi:10.1016/S0167-8396(01)00015-2.
 URL <http://www.sciencedirect.com/science/article/pii/S0167839601000152>
- [39] C. Birdsall, Particle-in-cell charged-particle simulations, plus Monte Carlo collisions with neutral atoms, PIC-MCC, IEEE Transactions on Plasma Science 19 (2) (1991) 65–85, number: 2 Conference Name: IEEE Transactions on Plasma Science. doi:10.1109/27.106800.
- [40] S. F. Biagi, Fortran program, magboltz v8.9, lxcnet (Jun. 2021).
- [41] J. F. J. Janssen, L. C. Pitchford, G. J. M. Hagelaar, J. v. Dijk, Evaluation of angular scattering models for electron-neutral collisions in Monte Carlo simulations, Plasma Sources Science and Technology 25 (5) (2016) 055026, publisher: IOP Publishing. doi:10.1088/0963-0252/25/5/055026.
 URL <https://doi.org/10.1088/0963-0252/25/5/055026>
- [42] L. M. Kishinevsky, Estimation of electron potential emission yield dependence on metal and ion parameters, Radiation Effects 19 (1) (1973) 23–27. doi:10.1080/00337577308232211.
 URL <http://www.tandfonline.com/doi/abs/10.1080/00337577308232211>
- [43] D. Hasselkamp, H. Rothard, K.-O. Groeneveld, J. Kemmler, P. Varga, H. Winter (Eds.), Particle Induced Electron Emission II, Vol. 123 of Springer Tracts in Modern Physics, Springer, Berlin, Heidelberg, 1992. doi:10.1007/BFb0038297.
 URL <http://link.springer.com/10.1007/BFb0038297>
- [44] J. Schou, Transport theory for kinetic emission of secondary electrons from solids, Physical Review B 22 (5) (1980) 2141–2174, publisher: American Physical Society. doi:10.1103/PhysRevB.22.2141.
 URL <https://link.aps.org/doi/10.1103/PhysRevB.22.2141>
- [45] J. F. Janni, Energy loss, range, path length, time-of-flight, straggling, multiple scattering, and nuclear interaction probability: In Two Parts. Part 1. For 63 Compounds Part 2. For Elements 1 Z 92, Atomic Data and Nuclear Data Tables 27 (4) (1982) 341–529. doi:10.1016/0092-640X(82)90005-5.
 URL <https://www.sciencedirect.com/science/article/pii/0092640X82900055>

- [46] J. F. Janni, Energy loss, range, path length, time-of-flight, straggling, multiple scattering, and nuclear interaction probability: In two parts. Part 1. For 63 compounds Part 2. For elements 1 Z 92, Atomic Data and Nuclear Data Tables 27 (2) (1982) 147–339. doi:10.1016/0092-640X(82)90004-3.
URL <https://www.sciencedirect.com/science/article/pii/0092640X82900043>

- [47] D. Hasselkamp, S. Hippler, A. Scharmann, Ion-induced secondary electron spectra from clean metal surfaces, Nuclear Instruments and Methods in Physics Research Section B: Beam Interactions with Materials and Atoms 18 (1-6) (1987) 561–565. doi:10.1016/S0168-583X(86)80088-X.
URL <https://linkinghub.elsevier.com/retrieve/pii/S0168583X8680088X>

- [48] R. C. Davidson, Equilibrium and stability of mirror-confined nonneutral E layers, Physics of Fluids 16 (12) (1973) 2199. doi:10.1063/1.1694287.
URL <https://aip.scitation.org/doi/10.1063/1.1694287>

- [49] F. Romano, S. Alberti, J.-P. Hogge, J. Genoud, G. Le Bars, J. Loizu, The TRapped Electrons eXperiment (T-REX), in: 2022 13th International Workshop on Non-Neutral Plasmas, Milano, To be published.
URL https://drive.google.com/file/d/1v77t-8oKMTDmqLGu6fKkSpaZL_cYSYcs/view